

PAPER • OPEN ACCESS

In situ x-ray analysis of misfit strain and curvature of bent polytypic GaAs–In_xGa_{1–x}As core–shell nanowires

To cite this article: Mahmoud Al-Humaidi *et al* 2022 *Nanotechnology* **33** 015601

View the [article online](#) for updates and enhancements.

You may also like

- [Erratum: Public Health England survey of eye lens doses in the UK medical sector \(*J. Radiol. Prot.* **34** 15\)](#)
E A Ainsbury, S Bouffler, M Cocker *et al.*
- [Corrigendum: Nonlocal optical effects on the Goos–Hänchen shifts at multilayered hyperbolic metamaterials \(2016 *J. Opt.* **18** 025104\)](#)
Chih-Wei Chen, Tingting Bian, Hai-Pang Chiang *et al.*
- [Discovery of ASKAP J173608.2–321635 as a Highly Polarized Transient Point Source with the Australian SKA Pathfinder](#)
Ziteng Wang, David L. Kaplan, Tara Murphy *et al.*



The Electrochemical Society
Advancing solid state & electrochemical science & technology

241st ECS Meeting

May 29 – June 2, 2022 Vancouver • BC • Canada

Abstract submission deadline: Dec 3, 2021





Connect. Engage. Champion. Empower. Accelerate.
We move science forward



Submit your abstract



In situ x-ray analysis of misfit strain and curvature of bent polytypic GaAs–In_xGa_{1–x}As core–shell nanowires

Mahmoud Al-Humaidi^{1,2} , Ludwig Feigl², Julian Jakob^{2,3} , Philipp Schroth^{2,3} , Ali AlHassan² , Arman Davtyan¹, Jesús Herranz⁴, Tasser Anjum¹, Dmitri Novikov⁵, Sonia Francoual⁵, Lutz Geelhaar⁴, Tilo Baumbach^{2,3} and Ullrich Pietsch¹

¹ Solid State Physics, University of Siegen, Walter-Flex Straße 3, D-57068, Siegen, Germany

² Institute for Photon Science and Synchrotron Radiation, Karlsruhe Institute of Technology, Hermann-von-Helmholtz-Platz 1, D-76344 Eggenstein-Leopoldshafen, Germany

³ Laboratory for Applications of Synchrotron Radiation, Karlsruhe Institute of Technology, Kaiserstraße 12, D-76131 Karlsruhe, Germany

⁴ Paul-Drude-Institut für Festkörperelektronik, Leibniz Institut im Forschungsverbund Berlin e.V., Hausvogteiplatz 5-7, 10117 Berlin, Germany

⁵ Deutsches Elektronen-Synchrotron, PETRA III, D-22607 Hamburg, Germany

E-mail: mahmoud.humaidi@kit.edu

Received 6 May 2021, revised 7 September 2021

Accepted for publication 24 September 2021

Published 20 October 2021



Abstract

Misfit strain in core–shell nanowires can be elastically released by nanowire bending in case of asymmetric shell growth around the nanowire core. In this work, we investigate the bending of GaAs nanowires during the asymmetric overgrowth by an In_xGa_{1–x}As shell caused by avoiding substrate rotation. We observe that the nanowire bending direction depends on the nature of the substrate's oxide layer, demonstrated by Si substrates covered by native and thermal oxide layers. Further, we follow the bending evolution by time-resolved *in situ* x-ray diffraction measurements during the deposition of the asymmetric shell. The XRD measurements give insight into the temporal development of the strain as well as the bending evolution in the core–shell nanowire.

Supplementary material for this article is available [online](#)

Keywords: core–shell, nanowire, *in situ*, XRD, strain, bending

(Some figures may appear in colour only in the online journal)

1. Introduction

During the past decades, semiconductor nanowires have been studied intensively, because of their wide range of potential applications in modern and future electronics and optoelectronic devices [1–5]. In particular, due to their high surface-

to-volume ratio, nanowires can sustain strain more efficiently compared to their planar counterparts. A conventional way to induce strain in nanowires is the combination of materials with different lattice parameters in the form of axial or radial heterostructures [6–8]. This strain modifies the optical properties of the respective device. For instance, growing an In_{0.50}Ga_{0.50}As shell around a thin lattice-mismatched GaAs nanowire core (with diameter <40 nm) causes a 40% reduction of the GaAs band-gap [9]. For the case of uniform shell distribution, the induced strain as well as the decrease in the band-gap are laterally uniform, and the nanowire remains



Original content from this work may be used under the terms of the [Creative Commons Attribution 4.0 licence](#). Any further distribution of this work must maintain attribution to the author(s) and the title of the work, journal citation and DOI.

Table 1. List of the investigated samples and the main properties required for this research.

Sample	Oxide type	Experimental technique	Nanowire length (nm) 100	Shell growth time (minute)	In content (%)
Sample 1	Native oxide	SEM	1800	30	30
Sample 2	Thermal oxide	SEM	1800	30	30
Sample 3	Native oxide	XRD+SEM	1200	20	15
Sample 4	Thermal oxide	XRD+SEM	1200	20	15
Sample 5	Thermal oxide	XRD+SEM	1200	11	15

straight. The realization of a spatially varying strain field can be induced by bending the nanowire which opens up new possibilities for strain and band-gap engineering [10–14]. Spontaneous nanowire bending can be achieved by an asymmetric shell growth around a lattice mismatched nanowire core [10, 15, 16]. The induced inhomogeneous strain distribution may cause the nanowire to bend fully backwards to contact either neighboring nanowires or the substrate serving as a new way to form electrical and optical interconnects [10]. Using molecular-beam epitaxy (MBE), the bending of the core-shell nanowires reported in [10] was achieved using a complicated growth scenario with substrate rotation and sequencing of group-III fluxes, to deposit the shell material on the same pre-define nanowire side resulting in nanowires bending to a defined direction. In other case, random nanowires bending along a non-defined direction was observed despite the fact that the template nanowires were rotating during lattice-mismatched shell growth [16].

In this research, we study the bending evolution of GaAs nanowires by growing an asymmetric $\text{In}_x\text{Ga}_{1-x}\text{As}$ shell with $x = 15\%$ and $x = 30\%$ nominal indium content using vapor-solid (VS) growth mode without performing substrate rotation. The growth was done by using a portable MBE (pMBE) chamber equipped with x-ray transparent beryllium windows. In order to trace the variation of the axial lattice parameter, we performed *in situ* XRD measurements on nanowires during shell deposition. These measurements give an access to the evolution of the strain and nanowire bending at the early stages which cannot be observed using the microscopic techniques, so far.

For this study we used samples of GaAs nanowire templates grown on Si(111) substrates covered by thin native oxide layer (<2 nm) on one hand and thicker thermal oxide (10–20 nm), on the other hand. However, in contrast to the shell deposition method used by Lewis *et al* [10], the entire process was carried out without sample rotation in order to maintain the consistent x-ray diffraction condition. We observed that nanowires grown on Si substrate with native oxide bend away from the group-V (As) flux whereas nanowires grown on Si with thermal oxide bend away from group-III (Ga) flux. This difference in the bending direction indicates a significant influence of the substrate oxide type, in addition to flux directions [17], to the preferable nanowire side facets for VS shell deposition. By means of scanning electron microscopy (SEM) we show that, despite the different bending directions, the nanowire curvature is comparable for both oxide types using similar MBE growth

conditions. These findings are confirmed by time-resolved *in situ* XRD measurements carried out on nanowire ensembles during shell deposition. Furthermore, the nanowire axial strain and curvature as functions of shell growth time show a nonlinear dependency at the early shell growth stages.

Finally, we extend our study by performing *in situ* XRD measurement on a single nanowire during the shell growth. The observed dependency of the single nanowire bending on shell growth time with the corresponding shell thickness is in agreement with the findings obtained from the nanowire ensembles.

2. Experimental details

2.1. Sample preparation

In our study, we used n-doped Si(111) substrates covered by naturally grown silicon oxide (referred to as ‘native oxide’ in the text) and thicker thermally-grown oxide layer (referred to as ‘thermal oxide’ in the text) with patterns of drilled nano-holes. The pattern structure is designed in such a way that we can investigate an ensemble of nanowires simultaneously, on one hand, and an individual nanowire, on the other hand. The two types of substrates require different sample treatments. The native oxide substrates pass through regular solvent cleaning (two rounds of dipping into Acetone, Isopropanol and Ultra-pure water baths in ultrasonic cleaner respectively). The patterned substrates with thermal oxide require hydro-fluoric (HF) acid etching following the same regular solvent cleaning used for native oxide substrates. The etching was done using 0.5% HF for 1 min to reduce the thickness of the naturally grown oxide on the substrate surface within the nano-holes. After oxide etching, the thermal oxide substrates were dipped into boiled ultra-pure water for 10 min for surface smoothing [18]. Afterwards, the substrates were degassed under the ultra-high vacuum condition at 300 °C for 30 min to get rid of solvent residuals before loading them into the MBE growth chamber. We investigated five samples in this study as listed in table 1 where the mean nanowire length (l_{NW}), shell thickness approximated from the calibration of the shell material growth in 2D planar system and the In concentration are listed there as well (the samples are numbered according to the performed study).

The growth of all samples was performed in a special pMBE chamber [19], which is designed for *in situ* x-ray characterization experiments at synchrotron radiation

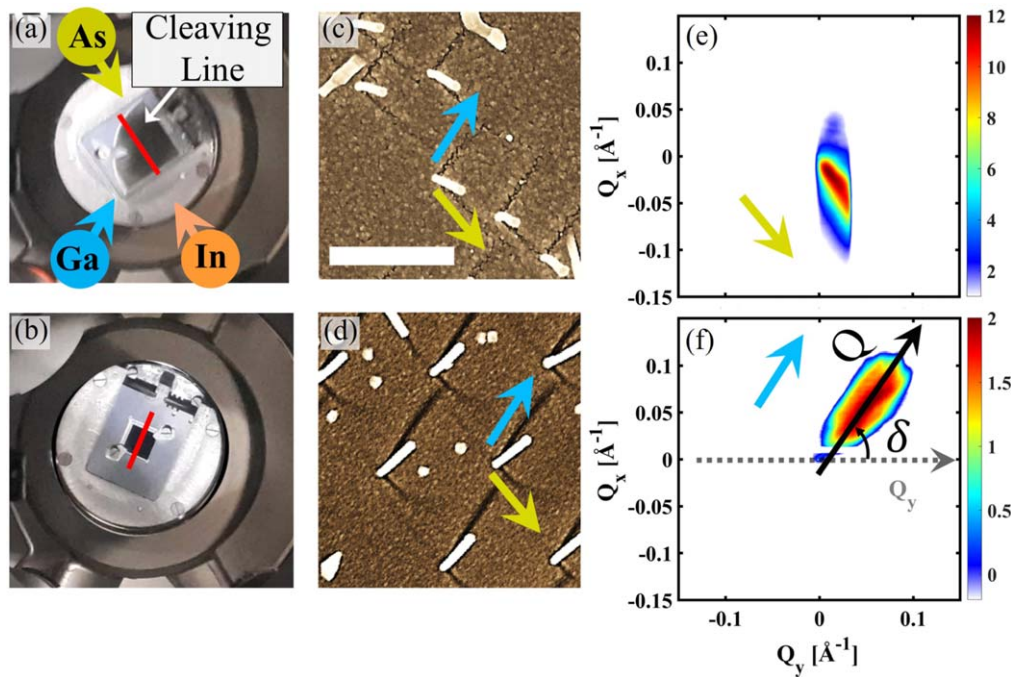


Figure 1. (a) and (b) Pictures of the geometrical arrangement of the growth material cells of the pMBE and the orientation of the quarter-inch substrate with native oxide layer (sample 1) and 1×1 cm patterned substrate with thermal oxide layer (sample 2), respectively. (c) and (d) Top-view SEM images of the bent nanowires of sample 1 and sample 2, respectively (the scale bar corresponds to $1 \mu\text{m}$). (e) and (f) Projection of GaAs(111) Bragg reflection on the (Q_x, Q_y) plane of RSM of the bent nanowires grown on substrate with native oxide layer (sample-3) and substrate with thermal oxide layer (sample 4) recorded after shell growth, respectively.

facilities. The pMBE chamber is equipped with solid source effusion cells of Ga and In, and valved cracker cell supplying As_4 . All cells are inclined to the substrate normal by $\Phi = 28^\circ$. The azimuthal angles are 60° between the Ga and the In cells and 120° between the Ga and the As_4 cells (see figure 1(a)).

The Si substrates of samples 2, 4 and 5 were covered by a 15–20 nm thick thermal oxide layer patterned with nano-hole arrays defined by electron-beam lithography. These nano-holes act as nucleation sites for Ga catalyst droplets for the epitaxial nanowire growth. The pattern consists of several equidistant $100 \times 100 \mu\text{m}^2$ large arrays of nano-holes arranged in a hexagonal grid. The separation between neighboring holes (pitch p) differs for each array, ranging from $p = 0.1 \mu\text{m}$ to $p = 10 \mu\text{m}$. Apart from the ensemble arrays, single nano-holes with $10 \mu\text{m}$ separation are drilled along a 1 mm straight line bordered by two etched markers to facilitate the illumination of single nanowire (see figure S1(i) in the supplementary materials available online at stacks.iop.org/NANO/33/015601/mmedia). More details about substrate preparation can be found in [18]. The sample layout enables the navigation on the substrate during the XRD measurements facilitating access to nanowire arrays (samples 2 and 4) and single nanowire (sample 5). The recipe to find a single nanowire using this substrate layout can be found in [20]. In this study we investigate the nanowires in arrays with pitch size $p = 1 \mu\text{m}$ in order to avoid the flux shadowing effect by the neighboring nanowires in case of lower pitch size [21].

Material fluxes were calibrated via the respective layer-by-layer growth on GaAs (001) substrate monitored by reflection high-energy electron diffraction. The readout of the

substrate temperature was calibrated to the temperature of Ga-oxide removal on epi-ready GaAs(001). Within the holes Ga catalyst droplets were formed at $T_{\text{sub}} \approx 630^\circ\text{C}$ by depositing Ga with an equivalent GaAs thickness of 50 monolayer (ML). Epitaxial VLS growth of the GaAs nanowire cores was initiated by supplying As and Ga simultaneously at $T_{\text{sub}} \approx 630^\circ\text{C}$ and using V/III ratio of 3 and a growth rate of 0.12 ML s^{-1} . The growth of the GaAs nanowires proceeded for 45 min for sample 2 and 30 min for samples 4 and 5 resulting in different mean nanowire lengths (l_{NW}) (see table 1).

For samples 1 and 3 which were grown on native oxide substrates, prior to nanowire growth procedure used for the other samples, Ga droplets were formed at $T_{\text{sub}} \approx 600^\circ\text{C}$ followed by annealing step for 15 min at $T_{\text{sub}} \approx 800^\circ\text{C}$ to evaporate the Ga droplets completely from the substrate surface. Randomly distributed nano-holes (i.e. nucleation sites) on the native oxide result from this procedure [22]. The growth time for the GaAs nanowires was 45 min for sample 1 and 30 min for sample 3 (see table 1).

To initiate the VS shell growth for all samples, first the Ga droplets at the nanowire apex were consumed to prevent any further axial VLS-growth. In the case of self-catalyzed GaAs nanowires, this is done by terminating the Ga supply while continuously supplying As at growth temperature. Afterwards, the substrate temperature and the material fluxes were adjusted to the desired parameters. The reduced substrate temperature T_{sub} (400°C (for samples 1–4) – 500°C (for sample 5)) and the higher V/III ratio ($\text{V/III} \approx 4$ (for sample 5) – 6 (for samples 1–4)) reduce the diffusion length

of the III-material favoring VS growth on the nanowire sidewalls.

The shell growth rate was chosen to be 0.04 ML s^{-1} which is equivalent to 0.8 nm min^{-1} for samples 1–4 and 0.25 ML s^{-1} (0.5 nm min^{-1}) for sample 5. The shell growth time was 30 min for samples 1 and 2, 20 min for sample 3, 20 min for sample 4 and 11 min for sample 5 as listed in table 1.

2.2. X-ray diffraction measurements

XRD serves as an ideal technique to investigate nanowire bending due to its high sensitivity to small changes in the crystal structure and orientation whereas these changes are indicated by the changes of the diffraction signal profile. Therefore, *in situ* XRD measurements were performed on GaAs nanowires during $\text{In}_{0.15}\text{Ga}_{0.85}\text{As}$ shell growth. The experiments were carried out at the German Electron Synchrotron (DESY-Hamburg). The *in situ* XRD measurements on sample 2 and sample 5 were performed at the Resonant Scattering and Diffraction beamline P09 [23] whereas nanowire arrays of sample 4 were measured at the *in situ* and Nano-x-ray diffraction beamline P23 [24]. Both beamlines are equipped with a heavy load goniometer which can withstand the weight of the pMBE. The beam was focused to a spot size of few microns ($1.5 \text{ }\mu\text{m}$ horizontal \times $5 \text{ }\mu\text{m}$ vertical) by means of compound refractive lenses which is essential to illuminate only the desired regions on the substrate. During all *in situ* XRD experiments, 2D pixel detectors were used for recording the diffracted signals. We measured reciprocal space maps (RSMs) in the vicinity of the GaAs(111) Bragg reflection in order to identify the bending direction in addition to measuring the nanowire bending angle (thus nanowire curvature) and the axial strain induced by the lattice-mismatched shell. Choosing a beam energy of 15 keV, the incident and scattering angles of the x-ray beam for the GaAs(111) Bragg reflection are 7.27° and 14.54° , respectively. These values are smaller than the maximum opening angle defined by the size of pMBE beryllium windows.

Rocking the GaAs(111) lattice planes around the Bragg angle of the respective reflection, the 3D intensity distribution of the Bragg reflection was recorded as a function of the incident angle and the horizontal and vertical angular ranges covered by the 2D detector. The angular coordinates are then translated to reciprocal space vectors using the equations listed in [25]. These vectors are Q_x , Q_y and Q_z and represent the 3D RSMs. Here Q_z is set parallel with the GaAs[111] nanowire growth axis and is sensitive to the variation in the axial lattice spacing (d_{111}), i.e. the axial strain $\epsilon_{||}$. The orthogonal components Q_x and Q_y , set parallel with the Si(111) plane of the substrate (Q_x is parallel with [0.11] and Q_y is parallel with [211]), are sensitive to changes in the crystal orientation (i.e. tilting and bending of the nanowire).

For samples 2 and 4, the shell growth and the XRD measurements were done in multiple cycles. At the end of each shell growth run, a RSM of the full 3D GaAs(111) Bragg reflection was recorded to track the evolution of the diffraction peaks caused by nanowire bending. For the single nanowire measurement (sample 5), we considered only few

selected 2D cuts through the 3D RSM to improve the time resolution of monitoring the XRD signal during nanowire bending.

The samples measured by XRD were intended to show a smaller bending compared to the samples inspected only by SEM because the diffraction signal could be followed only up to the maximum diffraction angle defined by the size of the pMBE beryllium windows. Therefore, the XRD data refer rather to the early stages of shell growth and nanowire bending.

3. Results and discussion

3.1. Bending direction

Since the substrate within the MBE during the growth is stationary (i.e. the alignment of the nanowire templates with respect to the MBE cells is fixed), the $\text{In}_x\text{Ga}_{1-x}\text{As}$ shell materials are deposited mainly on the nanowire side walls that face the material fluxes. The lattice parameters of the shell material is larger than that ones of the core, therefore, the induced mismatch axial strain (which is parallel to the nanowire axis $\epsilon_{||}$) causes the nanowire to bend away from the side at which the shell is deposited. The orientation of the material sources with respect to the Si substrate are shown in figure 1(a). For sample 1 (native oxide) we aligned the substrate in a way that a defined substrate edge is parallel to the direction of As flux (figure 1(a)). This edge is used as a reference for the later cleaving of the substrate (the red line in figure 1(a) indicate the cleaving edge). On the other hand, the thermal oxide substrate (sample 2) is aligned such that the cleaving edge directs to the Ga flux shown in figure 1(b). This alignment enables a directional reference for the SEM inspection and side-view SEM evaluation of nanowire curvature. In top-view SEM, the bent nanowires appear as elongated objects and thus allow the extraction the bending direction, thanks to our proper sample alignment in the chamber. As shown in figures 1(c) and (d) the bending direction differ for both samples.

In case of sample 1, the nanowires bend away from the As flux (yellow arrow in figure 1(c)), whereas in case of sample 2, the nanowires bend away from the Ga flux (blue arrow in 1(d)). This is an indication, that the position of the $\text{In}_x\text{Ga}_{1-x}\text{As}$ shell in case of the thermal oxide (sample 2) is given by the position of the Ga-source, whereas it is given by the position of the As-source in case of the native oxide (sample 1).

During the XRD measurements, several hundreds of nanowires were illuminated at the same time giving their mean properties and mean geometrical alignment. Using the same experimental conditions, the relative orientation of the nanowires geometry with respect to the reciprocal space geometry is consistent for all samples. Figures 1(e) and (f) show $Q_x Q_y$ projection of the 3D RSMs of the GaAs(111) reflection for samples 3 and 4. The elongation of the Bragg peak clearly evidences that the bending directions are

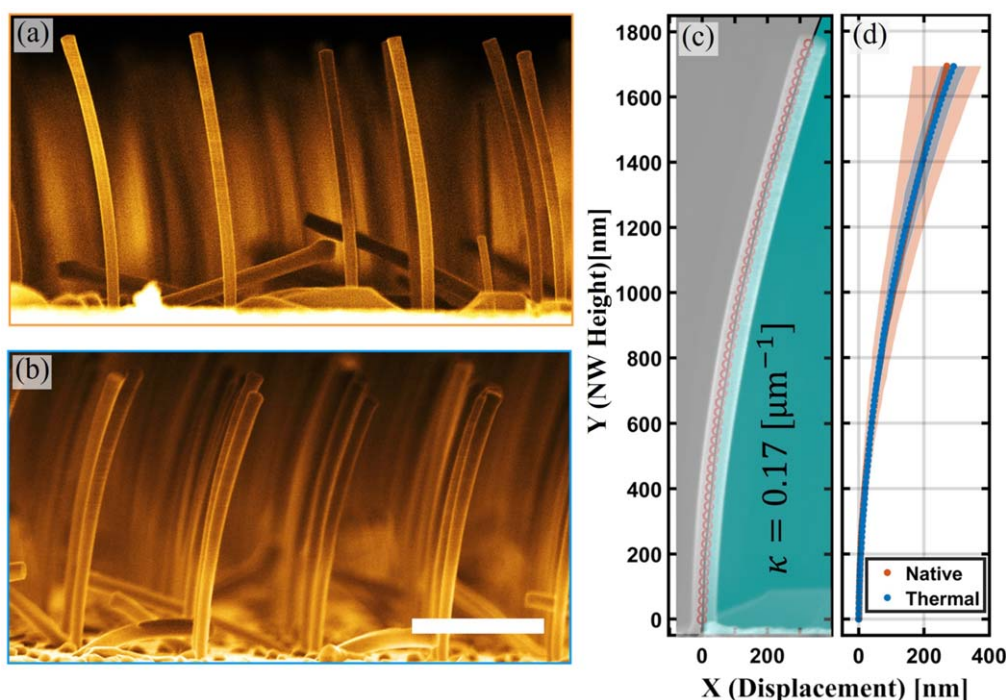


Figure 2. (a) and (b) Side-view SEM images of bent nanowires grown on Si substrate with native oxide (sample 1) and thermal oxide (sample 2), respectively (the scale bar corresponds to 1 μm). (c) Side-view SEM image of selected bent nanowire with extracted curvature profile and a circle fitting function for exemplary illustration of the SEM evaluation method of nanowires curvature. (d) Comparison of the curvature profile of the nanowires of the mentioned samples, where the shaded areas indicate the curvature variation and the lines are their mean values.

homogeneous within one substrate, but different for the two oxide types.

The careful alignment of the samples during growth further made it possible to cut the samples in such a way that side-view SEM investigations could be performed perpendicular to the bending directions. Figures 2(a) and (b) show side-view SEM images of bent core-shell nanowires grown on native oxide (sample 1) and thermal oxide (sample 2), respectively. The side-view images reveal that the curvature of the nanowires in sample 2 is more uniform than that of nanowires in sample 1. For quantitative analysis of the curvature, 47 nanowires from sample 1 and 40 nanowires from sample 2 were analyzed. Several data points were selected along the nanowire axis to obtain the bending profile. An exemplary visualization of this approach is demonstrated in figure 2(c). The curvature κ of this nanowire is about $0.17 \mu\text{m}^{-1}$ which was determined by fitting its profile using a circle function.

In figure 2(d) the mean nanowire bending profiles of both samples (i.e. samples 1 and 2) are plotted. Both samples have the same mean curvature as shown in red and blue lines, respectively. However, the local variation of the nanowire curvature is larger in case of native oxide substrates as shown by red and blue shades in figure 2(d). This finding can be explained by a larger variation of the GaAs nanowire diameters when grown on native oxide substrates. The overall evaluation proves the homogeneous curvature along the nanowire full length, which implies axial-homogeneity of shell deposition along the nanowire growth axis.

3.2. Bending evolution during shell growth

The analysis of the temporal evolution of the bending process and the axial strain was performed by *in situ* XRD experiments. The axial strain and bending can be distinguished by the changes of Bragg peak profile in the RSMs (see figure 3) as follows:

- Nanowire bending results in continuous change in the orientation of the GaAs(111) lattice planes resembled by broadening of the Bragg peak along a sphere in the RSM (see figures 1(e), (f) and 3(b), (f)).
- In case of no axial strain, the RSM sphere has a radius equals to the amplitude of Q_z which gives the inter-planar spacing (d_{111}) of the unstained nanowire crystal.
- When the axial strain is induced, the radius of the RSM sphere changes accordingly. In case of the tensile strain in the nanowire core (i.e. increment of d_{111} of GaAs crystal) the XRD signal shifts toward lower Q_z value (thus smaller radius of the RSM sphere). The broadening of the peak along Q_r as highlighted with gray arcs in figure 3(b) results from continues changes of the lattice parameter across the nanowire cross section (i.e. gradient strain).

To evaluate the spatial changes of the signal on the RSM sphere, we introduce two new reciprocal space vectors Q and Q_r which share the same origin as Q_x , Q_y and Q_z . The first vector Q is defined along the elongation of Bragg reflection as indicated by black arrow in figure 1(f). The amplitude of Q follows as $Q = \frac{|Q_y|}{\cos(\delta)}$ where $\delta = 56^\circ$ is the angle between the Bragg peak elongation direction (i.e. bending direction) and

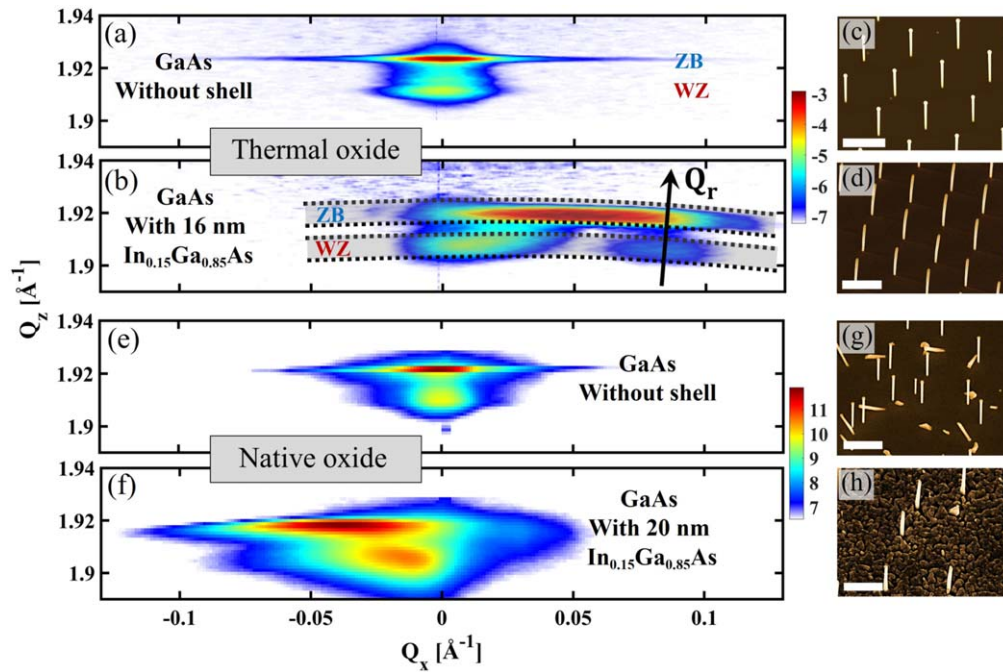


Figure 3. (a) and (b) GaAs(111) Bragg's reflection from nanowire ensembles on thermal oxide substrate (sample 4) projected on ($Q_x Q_z$) plane of RSMs recorded before and after the deposition of about 16 nm thick $\text{In}_{0.15}\text{Ga}_{0.85}\text{As}$ shell, respectively. (c) SEM images with 30° tilt-view of GaAs nanowire of a reference sample grown under same growth condition. (d) SEM images with 30° tilt-view of sample 4. (e) and (f) GaAs(111) Bragg's reflection from nanowire ensembles on native oxide substrate (sample 3) projected on ($Q_x Q_z$) plane. (g) and (h) Are the respective 30° tilt-view SEM images, where (g) is from a reference sample and (h) from sample 3 (All scale bars correspond to 1 μm).

Q_y . The other vector $Q_r = Q_z \sin(\beta)$ is tilted from Q_z by the bending angle β of the nanowire as indicated by black arrows in figure 3(b) (the illustration of the 3D arrangement of all RSM vectors can be seen in figure S2). Therefore, to measure the axial strain induced by the shell in the nanowire, the XRD signal must be evaluated along Q_r in the RSMs.

In order to record the whole nanowire bending, one needs to scan a wider range in reciprocal space compared to straight nanowires in order to cover the full elongation of the Bragg peak. The polytypism of GaAs nanowires can be utilized for a more accurate evaluation of the nanowire bending angle. In the first stages of Ga-assisted GaAs nanowire growth, the Ga droplet is unstable and small, resulting in the preferential growth of the WZ phase at the bottom of the nanowire (denoted by $\text{WZ}_{\text{Bottom}}$) and the inclusion of stacking faults [26]. During subsequent growth, the ZB phase and its rotational twin (TZB) are formed [27, 28]. To initiate radial VS growth, the axial VLS growth needs to be terminated by consuming the Ga catalyst. The consumption of the droplet changes the growth conditions and faulted ZB segments and WZ segments are formed on the top of the nanowire (denoted by WZ_{Top}) [21, 29]. Notably, when measuring the GaAs(111) Bragg reflection, ZB and its twin overlap at the same position in reciprocal space, and therefore cannot be distinguished, whereas the WZ is separated from the ZB signal.

Figures 3(a) and (b) show $Q_x Q_z$ projections of the GaAs (111) Bragg reflection of nanowires grown on the thermal oxide substrate (sample 4) before and after shell growth, respectively, indicating nanowire bending. In both figures, the XRD peaks of ZB and WZ are clearly discernible. Comparing

figures 3(a) and (b), the WZ and ZB peaks show significant changes, i.e. elongation of the ZB peak, and elongation and splitting of the WZ peak. SEM images with 30° tilt-view of the straight and bent nanowires are shown in figures 3(c) and (d), where the straight GaAs nanowires are from a reference sample grown under identical growth conditions of the studied sample.

To measure the mean curvature of the illuminated nanowires, one has to evaluate the elongation of the Bragg peaks along Q . To do so, we integrate the ZB and WZ signals on the RSM spheres with radii equal to the amplitude of Q_r for each polytype. Similar *in situ* XRD measurement was performed on nanowires grown on native oxide substrate (sample 3). The XRD signals of these wires before and after shell growth are shown in figures 3(e) and (f). The different elongation directions of the (111) Bragg peak for nanowires grown on thermal oxide substrate of sample 4 (figure 3(b)) and native oxide substrates of sample 3 (figure 3(f)) confirm the dependency of the bending direction on the oxide type. In further XRD study we focus on the nanowires grown on thermal oxide substrates (i.e. samples 4 and 5).

For nanowire that is straight and vertical to the substrate surface, all ZB lattice planes are flat and parallel in real space, which results in a sharp XRD peak at $(Q_x, Q_y) = 0 \text{ \AA}^{-1}$ (i.e. $Q = 0 \text{ \AA}^{-1}$) in RSM (figure 4(a)) with a width corresponds to the divergence of the probing x-ray beam. As soon as the nanowire starts to bend, the orientation of the lattice planes becomes a function of their position along the nanowire axis in real space causing broadening of the XRD peak in RSM. Figures 4(b) and (c) show the elongation of the XRD signal in

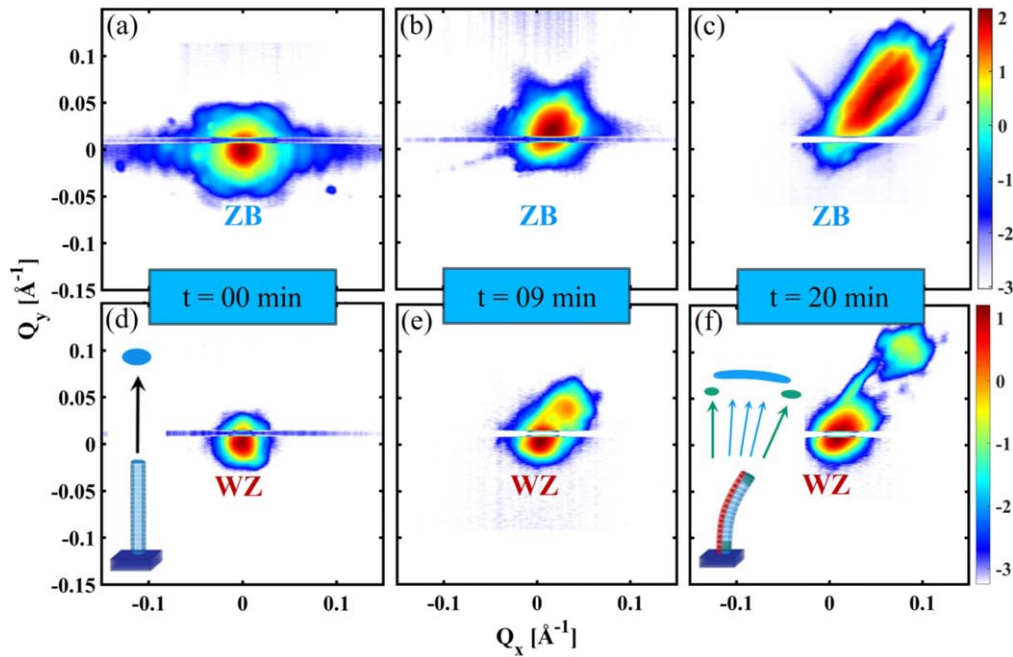


Figure 4. *In situ* XRD measurement of sample 4. (a)–(c) GaAs(ZB) Bragg's reflections before shell growth, after 9 min and 20 min of shell growth, respectively, (d)–(f) are the GaAs(WZ) Bragg's reflections at the same time stages.

$Q_x Q_y$ at different stages during shell growth time (before shell growth, after 9 min and after 20 min of shell growth). By estimating the integrated intensity ratio of the ZB peak to the total signal, it is apparent that the ZB phase represents about 80% of the crystal structure of the nanowire.

However, the XRD signal of the WZ phase behaves differently from the signal of ZB due to their distribution along the nanowire where WZ phase locates mainly at the bottom and the upper part of the nanowire. In straight nanowires, the two WZ segments (i.e. WZ_{Bottom} and WZ_{Top}) are located at the same position at $(Q_x, Q_y) = 0 \text{ \AA}^{-1}$ in reciprocal space (4(d)). As soon as the nanowire starts to bend, the WZ_{Top} peak moves accordingly, whereas the WZ_{Bottom} peak changes by negligible amount. This leads to peak splitting in reciprocal space (figures 4(e) and (f)).

Therefore, by knowing the mean length of the nanowires, the complete circular bending of the nanowire can be extracted from the separation of the two WZ peaks where this methods provide high accuracy.

The integrated intensities along Q and the resulting line profiles are represented in figures 5(a)–(c) for the three different growth stages demonstrated in figure 4 (i.e. before shell growth, after 9 and 20 min of shell growth). Before shell growth, the WZ (shaded in blue) and ZB (shaded in orange) peaks are both located at $Q = 0 \text{ \AA}^{-1}$. After 9 min of shell growth, the WZ peak splits into two separate ones. One peak remains close to $Q = 0 \text{ \AA}^{-1}$ with slight broadening towards higher Q values (shaded in blue in figures 5(b) and (c)), which we attribute to the WZ_{Bottom} segment. The second peak, centered at higher Q values, (shaded with yellow in figures 5(b) and (c)), originates from the WZ_{Top} segment. After 20 min of shell growth, the broadening of the ZB peak along Q figure 5(c) and the separation between the two WZ peaks

figure 5(f) increases further. The center of ZB peak during shell growth is located in between the two WZ peaks confirming the phase distribution along the nanowire. To track the evolution of the ZB and the two WZ peaks along Q as a function of shell growth time, the peak centers of the respective polytypes were extracted by fitting their XRD line profiles using Gaussian function, resulting in the plots in figure 5(d) (2D cuts of RSMs on Q and Q_z and the extracted line profiles along Q and Q_r are shown in figure S2). As the bending is found to be homogeneous the curvature κ of the bent nanowires can be described by a specific bending radius ($r = \kappa^{-1}$) and the bending angle β with respect to the normal of the substrate. The two parameters are related by $\beta = \kappa l_{NW}$ where l_{NW} denotes the nanowire length measured by SEM. The bending angle β is determined from the shifting of WZ_{top} XRD signal along Q using the basic relation $\tan(\beta) = \frac{Q(WZ_{top})}{Q_r}$ (as demonstrated in figure S3).

The tilt angle of (WZ_{top}) at the final stage (i.e. after 20 min of shell growth which corresponds to 16 nm shell thickness) is $\beta \approx 3^\circ$ considering the measured average length of the nanowires of $l_{NW} = 1100 \text{ nm}$. In this case the resulting final curvature is $\kappa \approx 0.047 \mu\text{m}^{-1}$. The distribution of both polytypes along the nanowire as well as the calculated nanowire bending at the three selected growth stages by our model of circular bending are visualized in figure 5(e).

By measuring the mean nanowire bending angle as function of shell growth time, the evolution of nanowire curvature during shell growth is plotted as function of shell growth time in figure 6(a). The curvature was determined by considering the mean nanowire length from a reference sample of straight nanowires shown in figure 6(b). For strain analysis, we consider only the strain induced in the GaAs(ZB) phase, since it is the prominent structure along the nanowire. The axial strain is extracted from the shift of the ZB peak along Q_r and

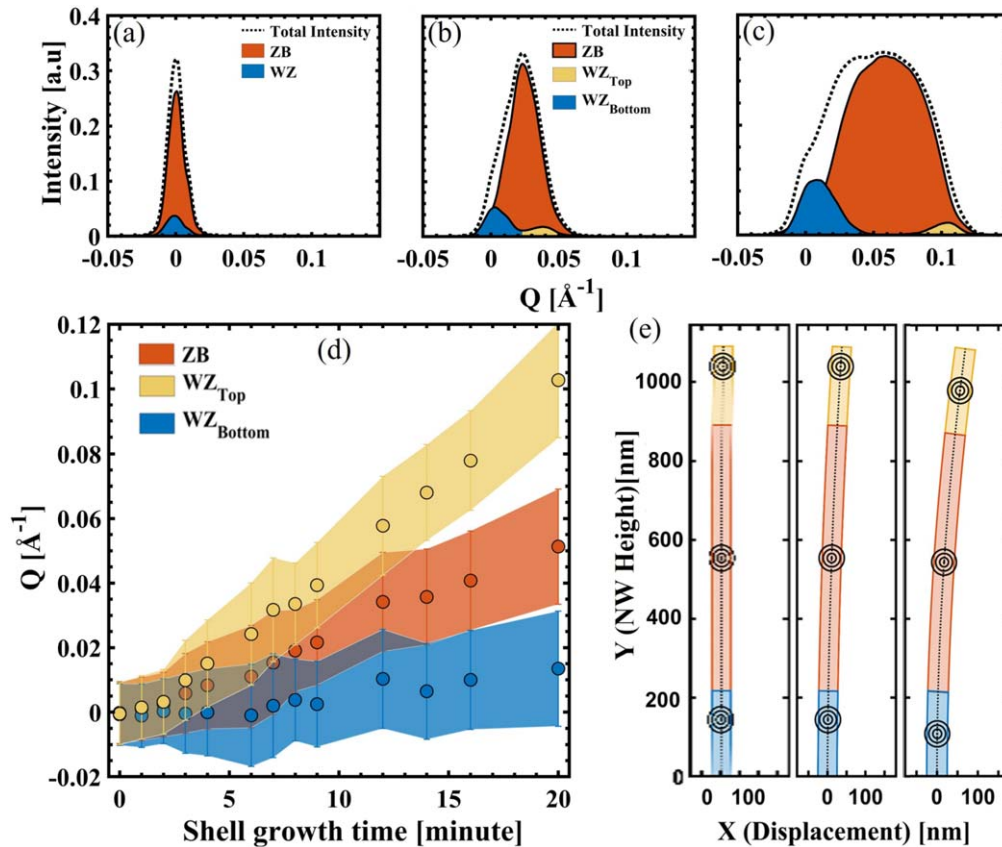


Figure 5. Profiling the XRD signals of sample 4. (a)–(c) are intensity profiles of the XRD signals of the respected polytypes at the three different growth stages as mentioned in figures 4(a)–(f) integrated along Q . (d) The peak positions of ZB, WZ_{Top} and WZ_{Bottom} along Q plotted as function of shell growth time. (e) Modeled phase stacking based on circular bending.

plotted as function of shell growth time where the broadening of the peaks was considered to estimate the strain variation as indicated by the bars as shown in figure 6(c) (see the supplementary materials).

From figures 6(a) and (c), it is evident that the evolution of the nanowire curvature and the strain are not linear with the shell growth time. During the first shell growth run of up to around 5 min of shell growth, minor curvature and strain occur. Exceeding the growth time of 5 min, the changes in nanowire curvature increases and reaches a value of about $\kappa \approx 0.05 \mu\text{m}^{-1}$ after 20 min of shell growth where the axial strain reaches a value of $\epsilon_{||} \approx 0.003$.

Nevertheless, the relation between the curvature and strain is linear as shown in figure 6(d) which implies that the linear elasticity of the studied core–shell system is still valid. The nonlinearity of relation between the shell growth time and the evolution of the strain and the curvature may be attributed to the changes of the growth dynamics during shell growth.

The axial lattice spacing (d_{111}) of the un-strained ZB can be measured from the diffraction peak on Q_r by $d_{111}(\text{GaAs}(\text{ZB})) = \frac{2\pi}{Q_r(\text{GaAs}(\text{ZB}))}$. The position of the Bragg peak on Q_r of the un-strained ZB at growth temperature is $Q_r(\text{GaAs}(\text{ZB})) = 1.9239 \text{\AA}^{-1}$ therefore $d_{111}(\text{GaAs}(\text{ZB})) = 3.2659 \text{\AA}$ and the corresponding lattice parameter $a_{(\text{GaAs}(\text{ZB}))} = 5.6566 \text{\AA}$. The measurement was performed at growth temperature and the thermal expansion of the GaAs

crystal is considered. However, using Vegard's law [30], the lattice parameter of the shell is $a_{(\text{In}_{0.15}\text{Ga}_{0.85}\text{As})} = 5.7174 \text{\AA}$ and which is the maximum allowed shared lattice parameter between the core and the shell, i.e. $\epsilon_{||}^{\max} = \frac{a_{(\text{In}_{0.15}\text{Ga}_{0.85}\text{As})} - a_{(\text{GaAs})}}{a_{(\text{GaAs})}} = 0.01$.

Therefore, considering the deduced linear relation between the strain and the curvature (figure 6(d)), the maximum predicted curvature that occurs at $\epsilon_{||}^{\max}$ will not exceed $\kappa \approx 0.25 \mu\text{m}^{-1}$. For this prediction the associated maximum effective shell growth time is ≈ 55 min that generates the axial strain and nanowire bending. However, this prediction holds only for the given core–shell system and it may differ for different parameters such as nanowire core diameter and In concentration as well as the inhomogeneity degree of the shell distribution.

To extend on our observations and get a deeper insight into the nanowire bending and strain evolution at the early stages of shell growth, we performed *in situ* XRD measurement on a single nanowire during shell growth. For this measurement, we scanned a smaller angular range in the vicinity of the GaAs(111) Bragg reflection in order to increase the time resolution to about 11 s. As the Si substrate is expected to be un-strained and straight, its Bragg reflection can be used as a reference to calculate the nanowire bending and the strain within its lattice. Accordingly, the Si(111) Bragg reflection was subsequently recorded after every 7 scans on GaAs(111) reflection. This explains the gaps in between each 7 scans in figures 7(a) and (b). The obtained 2D

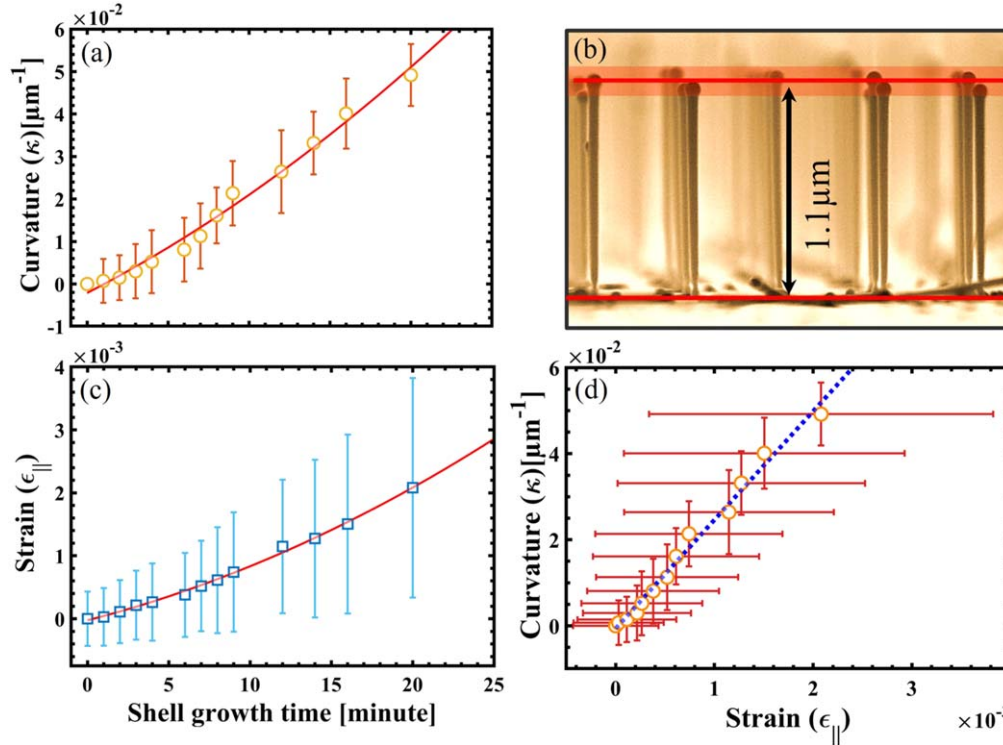


Figure 6. (a) Evolution of nanowire curvature as function of shell growth time. The curvature is measured by considering the nanowire length of a reference sample grown under identical growth conditions of the sample shown in (b). (c) Strain evolution in the ZB polytype as function of shell growth time. (d) Evolution of nanowire curvature as function of induced strain extracted from the *in situ* XRD measurement of sample 4.

RSMs and the line profiles extracted along Q_x and Q_z are shown in figure S4.

The growth was terminated after 11 min of shell growth corresponding to shell thickness of ≈ 5.5 nm. The position of Bragg peak on Q_x which indicates nanowire bending and the induced strain are plotted as functions of shell growth time in figures 7(a) and (b), respectively. It can be seen in 7(a) and (b) that both quantities pass through three phases during the early stages of shell growth can be explained as follows

- At phase-I, corresponding to about 2 min of shell growth time, no clear bending and minor strain is observed. At this stage, the first few monolayers of the growing shell (approximated to be with 1 nm in thickness) are subjected to a compressive strain to match the GaAs lattice and thus, these layers can scarcely influence the lattice parameter of the nanowire core as illustrated in figure 7(c).
- At phase-II, up to 4 min of shell growth time, a clear increase of the strain can be observed, while the nanowire bending angle slightly fluctuates. This observation can be explained by a quasi-uniform shell growth around the nanowire core facilitated by the smooth and un-strained nanowire side-facets. In this case the nanowire surface allows the shell material to diffuse freely and nucleate uniformly around the nanowire which results in a symmetric axial strain (uniform strain) that causes no nanowire bending as illustrated in figure 7(d).

- At phase-III, both bending angle and strain showed simultaneous increase. At this stage, as the strain increases the diffusivity of the shell material decreases accordingly. As a consequence of the decrement of the shell material diffusivity, the growth rate becomes higher on the nanowire facets that face the direct fluxes than the ones on the opposite side. Therefore, a non-uniform shell thickness around the nanowire results in varying strain across the nanowire cross section and thus nanowire bending as illustrated in figure 7(e). In this case, because of the induced asymmetric strain, the nanowire side that is subjected to higher tensile strain becomes more favorable for the continues shell growth than the other side of the nanowire which results in further increment of the growth rate on the tensile strained side. The opposite side of the nanowire, is subjected to two competitive sources of strain, where a tensile strain results from the shell material that may grow even with low growth rate and a compressive strain caused by nanowire bending. This regime may explain the nonlinear increment of the nanowire curvature and strain during shell growth as plotted in figures 6(a) and (b), respectively.

These assumptions can be supported by the changes of the strain evolution between phase-II and phase-III. It is clear that the increment of the strain is higher at phase-II (indicated by red arrow in figure 7(b)) than phase-III (blue arrow in figure 7(b)) where a certain amount of the strain is released by the nanowire bending. The strain variation across the

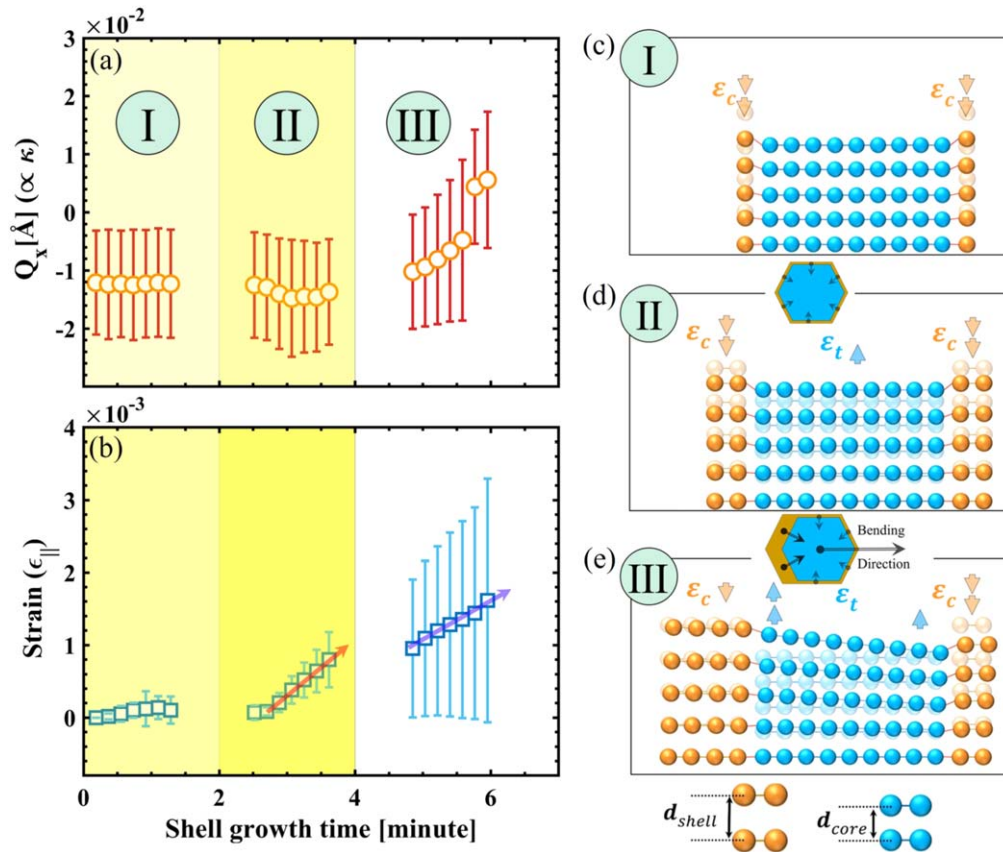


Figure 7. (a) Evolution of the bending angle of the single nanowire during shell growth. (b) Strain evolution in the ZB polytype of the single nanowire during shell growth of sample 5. (c) Animation of the three phases of shell growth indicating the axial strain of the core-shell nanowire and the resulting changes of the lattice plane orientation and the nanowire bending.

nanowire cross-section is represented by the bars in figure 7(b). This variation was estimated from the broadening of the XRD peak along Q_z as it can be seen by the line profile in figure S4(a).

4. Summary and outlook

As demonstrated in this research, uniform nanowire bending with controllable curvature along a definable bending direction can be achieved by avoiding substrate rotation during MBE growth of a lattice-mismatched shell. In this work, using Si substrates covered with native and thermal oxide, we observed different preferable bending directions of GaAs-In_xGa_{1-x}As core-shell nanowires. The bending direction which implies the preferable nanowire side facets for shell growth showed a clear dependency not only on the arrangement of the material sources, but also on the type of the oxide covering the substrates. For the given arrangement of the effusion cells in our MBE system we observed that the nanowires bend away from the direction of the Ga flux in case of using substrates covered with thermal oxide. On the other hand, nanowires grown on substrates covered with native oxide bend away from the direction of the As flux. This difference in the bending behavior requires further investigation and justification. By means of *in situ* XRD

measurements, we obtained a deep insight into the evolution of the induced axial strain and the resulting nanowire bending.

The evolution of the strain and nanowire bending showed nonlinear dependency as function of shell growth time. The nonlinearity of these functions was attributed to the changes of the growth dynamics during shell deposition due to the changes of the surface properties of the nanowire. The performed *in situ* XRD investigation on a single nanowire revealed that at the early shell growth stages, first the strain increases while the nanowire stays straight which suggests a uniform strain results from a homogeneous distribution of the lattice-mismatches shell around the nanowire core. Afterward, as the shell growth continues, nanowire bending starts to take place alongside with the increasing strain indicating changes in the homogeneity degree of the shell distribution around the nanowire.

Acknowledgments

The authors thank B Krause, A Weisshardt for their support at KIT, as well as S Dehm and the INT for access to the SEM. We are grateful to M Vogel and P auf dem Brinke for using the SEM at the Institute of Materials Engineering at the University of Siegen. We acknowledge DESY (Hamburg,

Germany), a member of the Helmholtz Association HGF, for the provision of experimental facilities. Parts of this research were carried out at PETRA III and we would like to thank D Reuther for helping setting up the experiment at the Resonant Scattering and Diffraction beamline P09 and A Khadiev for helping setting up the experiment at the *in situ* and Nano x-ray diffraction beamline P23 as well as M Lippmann for the support in the Clean Room. Other parts of this research were carried out at the DESY Nanolab and we would like to thank T F Keller, A Jeromin and S Kulkani for using the SEM. Furthermore, we are grateful to O Krüger and M Matalla (Ferdinand-Braun-Institut, Berlin) for electron-beam lithography and to A Tahraoui, S Meister and S Rauwerdink (Paul-Drude-Institut, Berlin) for substrate preparation.

This work was funded by BMBF project 05k16PSA with additional support within the framework of project MILAS.


Data availability statement

The data that support the findings of this study are available upon reasonable request from the authors.

ORCID iDs

Mahmoud Al-Humaidi  <https://orcid.org/0000-0001-7993-9720>

Julian Jakob  <https://orcid.org/0000-0002-4983-6533>

Ali AlHassan  <https://orcid.org/0000-0002-2924-4215>

References

- [1] Berg A, Yazdi S, Nowzari A, Storm K, Jain V, Vainorius N, Samuelson L, Wagner J B and Borgström M T 2016 *Nano Lett.* **16** 656–62
- [2] Gao Q et al 2014 *Nano Lett.* **14** 5206–11
- [3] Tomioka K, Yoshimura M and Fukui T 2012 *Nature* **488** 189–92
- [4] Bhuyan P D, Kumar A, Sonvane Y, Gajjar P N, Magri R and Gupta S K 2018 *Sci. Rep.* **8** 1–10
- [5] Tatebayashi J, Kako S, Ho J, Ota Y, Iwamoto S and Arakawa Y 2015 *Nat. Photon.* **9** 501–5
- [6] Grönqvist J, Søndergaard N, Boxberg F, Guhr T, Åberg S and Xu H Q 2009 *J. Appl. Phys.* **106** 053508
- [7] Johansson J and Dick K A 2011 *CrystEngComm* **13** 7175–84
- [8] Costas A, Florica C, Preda N, Kuncser A and Enculescu I 2020 *Sci. Rep.* **10** 1–12
- [9] Balaghi L, Bussone G, Grifone R, Hübner R, Grenzer J, Ghorbani-Asl M, Krashennnikov A V, Schneider H, Helm M and Dimakis E 2019 *Nat. Commun.* **10** 2793
- [10] Lewis R B, Corfdir P, Küpers H, Flissikowski T, Brandt O and Geelhaar L 2018 *Nano Lett.* **18** 2343–50
- [11] Fu X et al 2014 *Adv. Mater.* **26** 2572–9
- [12] Dietrich C P, Lange M, Klüpfel F J, von Wenckstern H, Schmidt-Grund R and Grundmann M 2011 *Appl. Phys. Lett.* **98** 031105
- [13] Lim B, Cui X Y and Ringer S P 2021 *Phys. Chem. Chem. Phys.* **23** 5407–14
- [14] Bartmann M G, Sistani M, Glassner S, Salem B, Baron T, Gentile P, Smoliner J and Lugstein A 2021 *Nanotechnology* **32** 145711
- [15] Greenberg Y, Kelrich A, Cohen S, Kar-Narayan S, Ritter D and Calahorra Y 2019 *Nanomaterials* **9** 1327
- [16] Gagliano L, Albani M, Verheijen M A, Bakkers E P and Miglio L 2018 *Nanotechnology* **29** 315703
- [17] van Treeck D, Fernández-Garrido S and Geelhaar L 2020 *Phys. Rev. Mater.* **4** 013404
- [18] Kupers H, Tahraoui A, Lewis R B, Rauwerdink S, Matalla M, Kruger O, Bastiman F, Riechert H and Geelhaar L 2017 *Semicond. Sci. Technol.* **32** 115003
- [19] Slobodskyy T, Schroth P, Grigoriev D, Minkevich A A, Hu D Z, Schaadt D M and Baumbach T 2012 *Rev. Sci. Instrum.* **83** 105112
- [20] Al Hassan A et al 2018 *Phys. Rev. Mater.* **2** 014604
- [21] Schroth P, Jakob J, Feigl L, Kashani S M M, Pietsch U and Baumbach T 2018 *MRS Commun.* **8** 871–7
- [22] Tauchnitz T, Nurmamyrov T, Hübner R, Engler M, Facsko S, Schneider H, Helm M and Dimakis E 2017 *Cryst. Growth Des.* **17** 5276–82
- [23] Stremper J, Francoal S, Reuther D, Shukla D K, Skaugen A, Schulte-Schrepping H, Kracht T and Franz H 2013 *J. Synchrotron Radiat.* **20** 541–9
- [24] DESY *in situ* and nano x-ray diffraction beamline (<https://photon-science.desy.de/facilities>)
- [25] Pietsch U, Holý V and Baumbach T 2004 *High-Resolution X-Ray Scattering* (Berlin: Springer)
- [26] Shtrikman H, Popovitz-Biro R, Kretinin A, Houben L, Heiblum M, Buksa M, Galicka M, Buczko R and Kacman P 2009 *Nano Lett.* **9** 1506–10
- [27] Rieger T, Lepsa M I, Schapers T and Grützmacher D 2013 *J. Cryst. Growth* **378** 506–10
- [28] Yamashita T, Akiyama T, Nakamura K and Ito T 2010 *Japan. J. Appl. Phys.* **49** 0550031
- [29] Jacobsson D, Panciera F, Tersoff J, Reuter M C, Lehmann S, Hofmann S, Dick K A and Ross F M 2016 *Nature* **531** 317–22
- [30] Denton A R and Ashcroft N W 1991 *Phys. Rev. A* **43** 3161–4